Engine Cycle Comparison for Alternative Propellant Nuclear Thermal Propulsion Engines

Daria Nikitaeva[1], Corey D. Smith[2], Matthew Duchek[3]

[1] *Aerospace Systems Engineer, Advanced Projects, Analytical Mechanics Associates, Huntsville, AL, 35806*

[2] *Nuclear Engineer, Advanced Projects, Analytical Mechanics Associates, Huntsville, AL, 35806*

[3] *Aerospace Engineering Manager, Advanced Projects, Analytical Mechanics Associates, Denver, CO, 80211*

A modular Nuclear Thermal Propulsion (NTP) engine modeling suite (X-NTP) was coded in Simulink to analyze various engine cycle configurations and propellants. This model was validated and used for previous studies involving alternative propellants for NTP engines. The current study compared hydrogen-based NTP (H-NTP) with ammonia-based Alternative propellant NTP (A-NTP) engines with expander and bleed cycle configurations. Based on prior work, the bleed cycle configuration was modified to yield a feasible result. The assumption that was made was that the Testing Reference Design (TRD) reactor will be used for all cases and that the difference in fuel loading fractions will be enough to offset any differences in the neutronics caused by switching the propellant. This work provided and compared propellant state points throughout the cycles as well as the key performance parameters. The conclusion was that bleed cycles for H-NTP engines are advantageous over expander cycles in terms of maximum system pressure, cycle simplicity, and potentially engine mass. Conversely, expander cycles are more advantageous for A-NTP engines according to the same scope of parameters. Future work will analyze reactor designs that are different from the TRD and use neutronics software integrated with the X-NTP model to provide higher fidelity results.

I. INTRODUCTION/BACKGROUND

Nuclear Thermal Propulsion (NTP) is an in-space propulsion system which underwent significant development in the United States 1950s through the early 1970s during the Project Rover and Nuclear Engine for Rocket Vehicle Application (NERVA) programs. The goal of these two programs was to create a propulsion system capable of transporting humans to Mars and provide a reusable lunar shuttle. Unlike chemical propulsion, NTP does not depend on combustion of an oxidizer and fuel to produce thrust; instead, a propellant is pumped into a nuclear reactor and heated to high temperatures before being expelled through a nozzle. Essentially, the NTP-based engine is a monopropellant system [1]. This allows for the theoretical use of any fluid to be used as a propellant if it is compatible with the neutronics inside the reactor and the materials do not exhibit significant degradation throughout the useful life of the engine at the high temperatures and pressures that are typically found inside the reactor core.

Hydrogen is commonly considered as a propellant for NTP engines due to its low molecular weight which maximizes the benefit of the monopropellant capability by maximizing the achievable specific impulse (a measure of propellant efficiency in rocket engines). Hydrogen-based NTP engines in literature have been referred to as H-NTP. Although hydrogen has some favorable properties such as very low molecular weight and a critical point with relatively low pressure and temperature (1.3 MPa and 33 K, respectively), it has high specific heat capacity and

low density. These properties exhibit drawbacks in both an engine and space transportation vehicle context, respectively.

1. High Specific Heat Capacity

Hydrogen has excellent energy storage properties given its extremely high constant pressure specific heat. The result of this is that even though hydrogen can very effectively cool down the reactor, more nuclear thermal power is needed to raise hydrogen's temperature than for other substances to unlock its high specific impulse potential.

2. Low Density

A substance with low density requires large volume tanks that need to be transported into orbit. This results in higher vehicle dry mass to accommodate the volume occupied by this propellant. Low density also has a large impact on pressure losses within the ducts and lines of an engine's regenerative cooling and turbomachinery systems due to the resulting high volumetric flow rate. Pressure losses, when considering only fluid properties, are primarily driven by the flow velocity as indicated by the Darcy–Weisbach pressure loss formulation and are secondarily driven by the fluid viscosity as indicated by Wood's friction factor correlation [2]. The consequences of these pressure losses are that the turbomachinery must be able to make up for these pressure losses and the duct diameter be larger than for an otherwise lower flow rate and/or denser fluid.

An alternate propellant-based NTP (A-NTP) engine was considered by previous work to address hydrogen's high specific heat capacity and low density recommended using anhydrous ammonia as the propellant [3]. This fluid is around ten times denser than hydrogen and has a specific heat capacity around seven times less than hydrogen. However, ammonia has a molecular weight of 17.031 g/mol which is significantly higher than hydrogen's of 2.016 g/mol resulting in a predicted specific impulse of about a third of hydrogen [4]. Although an ammonia-based vehicle architecture results in a comparatively much heavier wetted mass than a hydrogen-based architecture, for certain missions, the storability of the propellant may outweigh the mass penalty [5]. Previous work examined both expander and hot bleed cycles for hydrogen and ammonia-based A-NTP engines. Although comparisons were made regarding the performance and the difference in the engine cycle flow schedule, the previous work only provided a high level overview of the engine performance of different configurations of reactors and used steady state power levels. [3] This work will take a closer look at the engine state points and performance levels and provide a more thorough investigation on the differences between hydrogen and ammonia propellants and their associated engine cycles. Furthermore, previous work identified that the hot bleed cycle or a combined cold/hot bleed cycle for ammonia-based A-NTP engines will be infeasible due to high chamber temperatures and turbine material limitations as well as the phase of ammonia being liquid prior to entering the reactor core. [3] This work will re-examine this conclusion by introducing a preheating stage in the bleed cycle analysis.

II. X-NTP MODEL OVERVIEW

Prior work developed H-NTP and A-NTP power balance models in Simulink with separate models used for the different engine cycle configurations and propellants [3]. The present work used the physics models of these power balance models; however, the model configuration was changed to be modular. This added modularity allows for the selection of different options which control the flow of the propellant throughout the engine and thereby changing the engine cycle

entirely. Furthermore, built in propellant modularity allows for the selection of a variety of different fluids to be used in this model and effectively combining the H-NTP and A-NTP models into a single modular X-NTP model.

A. Governing Physics

This section provides a brief overview of the governing physics used in the X-NTP model. Further details such as derivations and reasoning for the selection of the included correlations have been described in detail by previous works [3,6–9].

1. Turbomachinery

The pump work $\dot{W}_p$ and rotating velocity ω are shown in Eq. 1 and Eq. 2, respectively which are based on the pump mass flow rate $\dot{m}_p$, fluid density ρ, pressure P, physical pump diameter D_p, and specific speed of the pump n_{s_p}. Eq. 3 describes the specific diameter which can be used to extract the pump efficiency from a contour plot [10].

$$\dot{W}_p = \frac{\dot{m}_p(P_{out} - P_{in})}{\rho} \quad \text{Eq. 1}$$

$$\omega = \frac{n_{s_p}\left(g_0 H_p\right)^{3/4}}{\sqrt{\dot{\forall}_p}} = \frac{n_{s_p}(P_{out} - P_{in})^{3/4}}{\rho^{1/4}\sqrt{\dot{m}_p}} \quad \text{Eq. 2}$$

$$d_{s_p} = \frac{D_p\left(g_0 H_p\right)^{1/4}}{\sqrt{\dot{\forall}_p}} = \frac{D_p[\rho(P_{out} - P_{in})]^{1/4}}{\sqrt{\dot{m}_p}} \quad \text{Eq. 3}$$

Similarly, the affinity laws for the turbine are expressed through the fluid enthalpy instead of the pressure. The expression for the required turbine specific speed n_{s_t} and specific diameter d_{s_t} (based on the physical turbine diameter D_t) are shown in Eq. 4 and Eq. 5, respectively.

$$\dot{W}_p = \frac{\dot{m}_p(P_{out} - P_{in})}{\rho} \quad \text{Eq. 4}$$

$$\omega = \frac{n_{s_p}\left(g_0 H_p\right)^{3/4}}{\sqrt{\dot{\forall}_p}} = \frac{n_{s_p}(P_{out} - P_{in})^{3/4}}{\rho^{1/4}\sqrt{\dot{m}_p}} \quad \text{Eq. 5}$$

The turbines are throttled by controlling the mass flow rate which can be determined by using a modified and simplified expression of the 1st Law of Thermodynamics for an open system as shown in Eq. 6. The turbine efficiency can be found from a contour plot. Using the isentropic efficiency, the isentropic outlet enthalpy can be found by using Eq. 7 and, in conjunction with the inlet entropy, the outlet pressure can be found to determine the turbine pressure ratio via fluid properties look-up table [11].

$$\dot{m}_t = \left(\dot{W}_{shaft} - \dot{Q}_{in}\right)^{3/5}\left(\frac{n_{s_t}\sqrt{\rho}}{\omega}\right)^{4/5} \quad \text{Eq. 6}$$

$$\eta_t = \frac{h_{in} - h_{out}}{h_{in} - h_{out_s}} \rightarrow h_{out_s} = h_{in} - \frac{h_{in} - h_{out}}{\eta_t} \quad \text{Eq. 7}$$

2. Cooling Channel Flow

The cooling channel analysis is based on a nodal model shown in Figure 1. Here, the energy coming into node i of length Δx is the fluid enthalpy $\dot{m}h_i$ as well as the heat allocated to this node δQ_i. It is assumed that all δQ_i goes into the fluid to result in the energy leaving the node of $\dot{m}h_{i+1}$. This leads to a temperature rise of ΔT and a node exit temperature of T_{i+1}. The Westinghouse convective heat transfer coefficient $\hbar$ for hydrogen is used as recommended by the industry [12] and is shown in Eq. 8. The Gnielinski correlation is used for alternative propellants as it captures a large range of Reynolds and Prandtl numbers and is shown in Eq. 9. The ratio of the bulk Prandtl number Pr to the Prandtl number found at the channel wall Pr_w and evaluated at the channel surface temperature is used to accommodate for the large temperature differences found in the cooling channels.

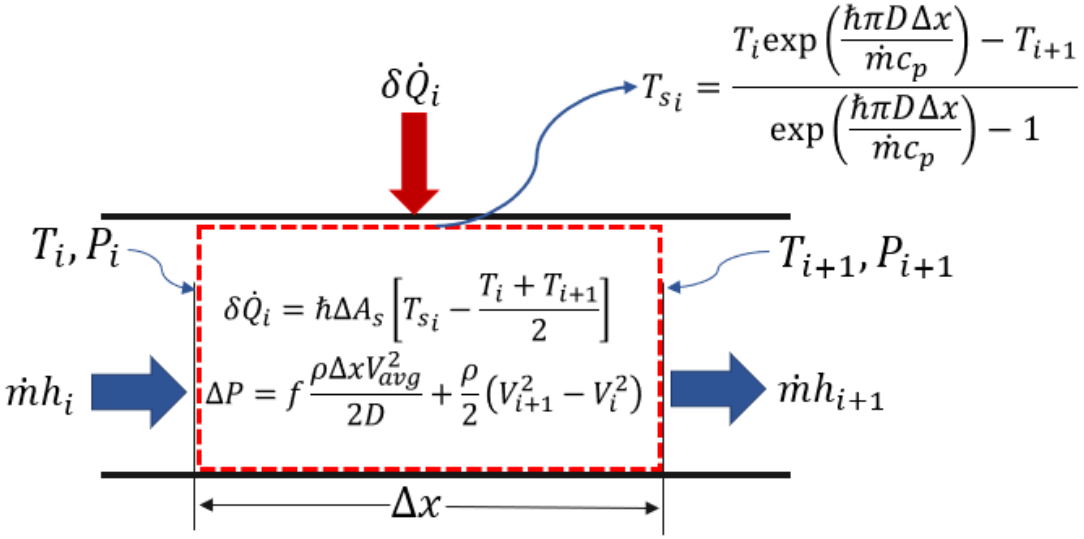

Figure 1: Reactor Channel Nodal Heat Transfer Schematic

$$\hbar = 0.025\frac{k}{D}Re^{0.8}Pr^{0.4}\left[1 + 0.3\left(\frac{D}{\sum_{j=1}^{i}\Delta x}\right)^{0.7}\right]\left(\frac{2T_{s_i}}{T_i + T_{i+1}}\right)^{-0.55} \quad \text{Eq. 8}$$

$$\hbar = \frac{K}{D}\frac{\frac{f}{8}Pr(Re - 1000)}{1 + 12.7\left(\frac{f}{8}\right)^{1/2}\left(Pr^{2/3} - 1\right)}\left(\frac{Pr}{Pr_w}\right)^{0.11} \quad \text{Eq. 9}$$

The surface temperature of the node T_{s_i} and the exit temperature T_{i+1} are found by solving Eq. 10 and Eq. 11 simultaneously. The pressure drop within the node is found by incorporating

both frictional and momentum/acceleration pressure losses as shown in Eq. 12. For both the frictional pressure losses and the Gnielinski correlation, the friction factor that is recommended by industry [12] is that of Churchill for which the expression together with the coefficients A and B are shown in Eq. 13.

$$\delta Q_i = \hbar \Delta A_s \left[T_{s_i} - \frac{T_i + T_{i+1}}{2} \right] \quad \text{Eq. 10}$$

$$T_{s_i} = \frac{T_i exp\left(\frac{\hbar \pi D \, \Delta x}{\dot{m} c_p}\right) - T_{i+1}}{exp\left(\frac{\hbar \pi D \, \Delta x}{\dot{m} c_p}\right) - 1} \quad \text{Eq. 11}$$

$$\Delta P = f \frac{\rho \Delta x V_{avg}^2}{2D} + \frac{\rho}{2}(V_{i+1}^2 - V_i^2) \quad \text{Eq. 12}$$

$$f_{CH} = 8 \left[\left(\frac{8}{Re}\right)^{12} + \frac{1}{(A+B)^{1.5}} \right]^{1/12}$$

Where:

$$A = \left[2.457 \ln \left(\frac{1}{\left(\frac{7}{Re}\right)^{0.9} + 0.27 \frac{\varepsilon}{d}} \right) \right]^{16} \quad \text{Eq. 13}$$

$$B = \left(\frac{37530}{Re}\right)^{16}$$

The maximum fuel temperature at the i^{th} node is calculated by using the heat transfer through an anulus formulation shown in Eq. 14. Since each fuel element has multiple channels, for analysis simplification, an equivalent cross sectional fuel area is allocated per channel. The resulting equivalent outer fuel diameter $d_{c_{out}}$ is shown in Eq. 15 which is based on the diameter of the entire fuel element d_f, the number of propellant flow channels per fuel element n, and the internal channel diameter $d_{c_{in}}$.

$$T_{f_{max_i}} = \frac{\delta \dot{Q} \ln\left(\frac{d_{c_{out}}}{d_{c_{in}}}\right)}{2\pi k_f \Delta x} + T_{s_i} \quad \text{Eq. 14}$$

$$d_{c_o} = \sqrt{\frac{d_f^2 - n d_{c_i}^2}{n} + d_{c_i}^2} \quad \text{Eq. 15}$$

3. Nozzle Fluid Dynamics and Heat Transfer

Standard isentropic quasi-one-dimensional compressible flow equations are used to model the flow inside the nozzle. The equations for the temperature (Eq. 16), pressure (Eq. 17), mass flow rate (Eq. 18), area ratio (Eq. 19), thrust (Eq. 20), and specific impulse (Eq. 21) are provided.

$$\frac{T_0}{T_e} = 1 + \frac{\gamma - 1}{2} M_e^2 \quad \text{Eq. 16}$$

$$\frac{P_0}{P_x} = \left(1 + \frac{\gamma - 1}{2} M_x^2\right)^{\frac{\gamma}{\gamma - 1}} \quad \text{Eq. 17}$$

$$\dot{m}_{max} = P_0 A^* \sqrt{\frac{\gamma}{RT_0}} \cdot \left(\frac{2}{\gamma + 1}\right)^{\frac{\gamma+1}{2(\gamma-1)}} \quad \text{Eq. 18}$$

$$\frac{A^*}{A_x} = M_x \left[\frac{\frac{\gamma + 1}{2}}{1 + \frac{\gamma - 1}{2} M_x^2}\right]^{\frac{\gamma+1}{2(\gamma-1)}} \quad \text{Eq. 19}$$

$$F = \eta_{noz}[\dot{m} v_e + (P_e - P_a) A_e] \quad \text{Eq. 20}$$

$$I_{sp} = \frac{F}{\dot{m} g} \quad \text{Eq. 21}$$

The regenerative cooling channel heat transfer and pressure losses use the same methodology as was described in Section II.A.2. However, the heat transfer from the plume to the nozzle is modelled by Bartz's convective heat transfer coefficient shown in Eq. 22 where σ is the dimensionless boundary layer factor which is expressed in Eq. 23 where s is the exponent inside the Power-Law Force equation shown in Eq. 24. s is determined by using Eq. 24 alongside a reference state (throat conditions) and a state of interest (at location x).

$$\hbar_x = \frac{0.026}{D_t^{0.2}} \left(\frac{\mu_x^{0.2} c_p}{Pr^{0.6}}\right)_0 \left(\frac{\dot{m}}{A_t}\right)^{0.8} \left(\frac{D_t}{r_c}\right)^{0.1} \left(\frac{A_t}{A_x}\right)^{0.9} \sigma \quad \text{Eq. 22}$$

$$\sigma = \left\{\left[\frac{1}{2}\frac{T_{s_o}}{T_0}\left(1 + \frac{\gamma - 1}{2} M_x^2\right) + \frac{1}{2}\right]^{0.8 - \frac{s_x}{5}} \left[1 + \frac{\gamma - 1}{2} M_x^2\right]^{\frac{s_x}{5}}\right\}^{-1} \quad \text{Eq. 23}$$

$$\mu_x = \mu^* \left(\frac{T_x}{T^*}\right)^{s_x} \quad \text{Eq. 24}$$

The nozzle contour is also an important aspect that pertains to the effectiveness of the convective heat transfer within the regenerative cooling section. This was modeled by converging and diverging quadratic equations connected by a circle at the throat. The Appendix of this paper provides the complete derivation of the equations that are used in the X-NTP model.

B. Engine Model Configuration

The X-NTP model is meant to be a modular NTP engine design suite with the ability to pick and choose the engine cycle, flow schedule, and components utilized. The general schematic of the model is shown in Figure 2. The two large blocks on top and on the bottom function as signal distributors to the component blocks in the middle. Each component block has its own set of governing equations with a zoomed in high-level view of an arbitrary block shown in Figure 3. This provides the power to reassemble the engine components easily into alternative cycle configurations without recoding the components.

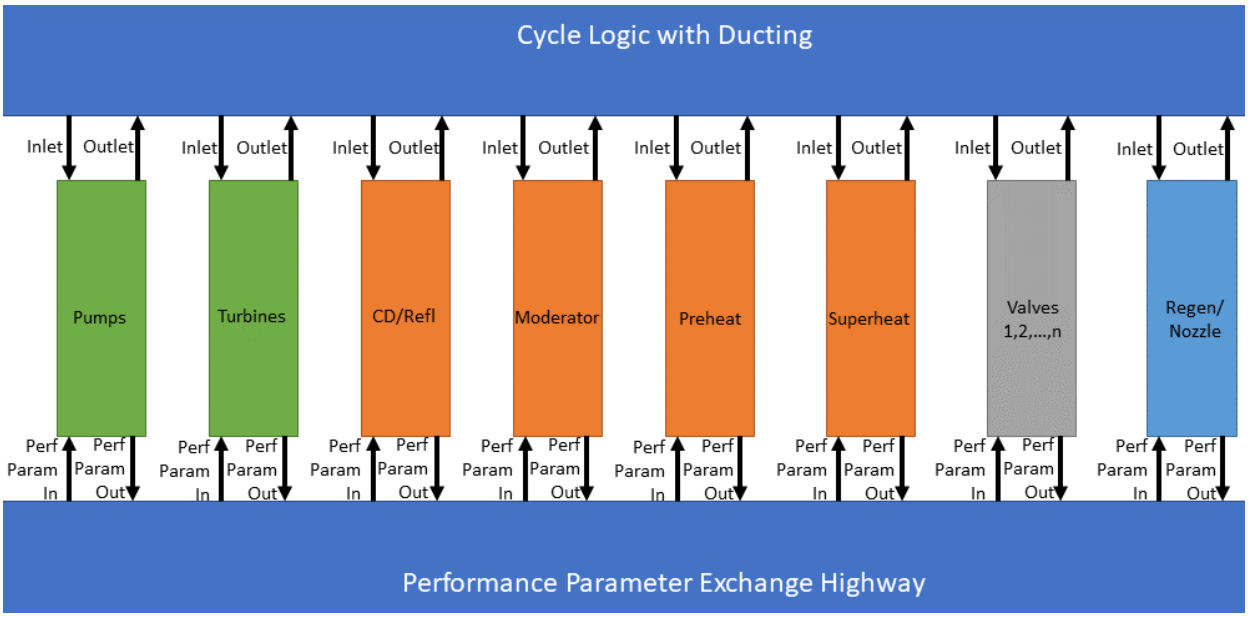

Figure 2: X-NTP High-Level Schematic

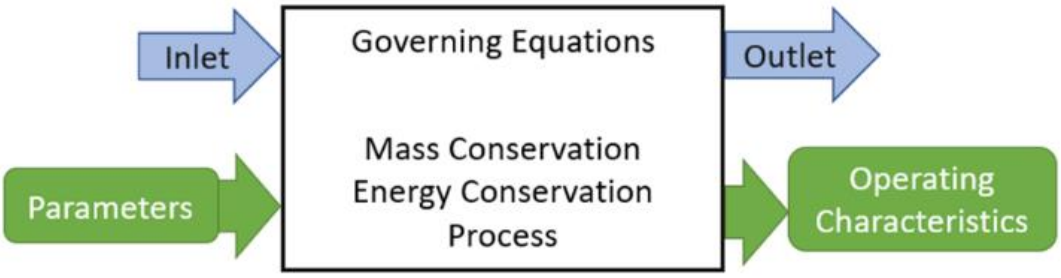

Figure 3: Arbitrary Engine Component Schematic

The "Cycle Logic with Ducting" block takes user inputs such as the desired flow schedule and cycle and distribute the inputs and outputs of the component blocks to match the desired resulting engine cycle. Furthermore, this block also incorporates the ducting as well as any flow turns involved and thus provide a pressure loss estimate. The "Performance Parameter Exchange Highway" block takes parameters from the existing blocks such as the required pump work, shaft speed, and net reactor heat and redistributes them to the necessary components. Unlike the "Cycle

Logic with Ducting" block, the "Performance Parameter Exchange Highway" block does not depend on user inputs and redistributes the performance parameters in a static manner.

C. Reactor Considerations

Common engineering practice related to engine analyses treats the reactor subsystem as a heat exchanger without accounting for the in-depth multiphysics of the neutronics. This work addresses this assumption through the development of high-fidelity reactor physics models based on NASA's Testing Reference Design (TRD) using the Monte Carlo probabilistic neutron transport tool Serpent [13]. The baseline TRD is composed of a moderator block H-NTP configuration with internally-cooled circular fuel assemblies serving the purpose of superheating the hydrogen working fluid prior to reaching the nozzle chamber. While A-NTP engine cases utilize the TRD for its geometry and power level, a variation to the flow schedule and the reactor modeling algorithm is implemented to include fuel assembly preheating following the moderator and reflector flow. This update is imperative for propellant choices that will not reach a supercritical state prior to the turbine without additional enthalpy insertion, such as ammonia. While simplistic to model from a thermal hydraulic perspective, current NTP designs are not readily capable to enable preheating from a thermostructural and possible neutronics perspective.

For preheated A-NTP engines, the fluid density and temperature profile will vary significantly across the radial geometry of the active core which will vary the input file structure and underlying assumptions. To inform these inputs to the engine model, a general Serpent file is simulated with an assumed temperature and density shape to provide power distributions in the fuel, moderator, and reflector components. Following inclusion into the cooling channel analysis using the methodology described in previous sections of this report, updated thermal hydraulic conditions are provided to Serpent until a convergence parameter is reached. A comparable algorithm is utilized for H-NTP as well, but the radial thermophysical property variation is substantially less impactful on the final criticality and other pertinent results. This process is outlined in Figure 4.

An example of the resulting average power distribution curve is shown in Figure 5 where the top of the reactor is on the right-hand-side. Here, the values have been omitted for secure distribution purposes. Furthermore, this average distribution curve is the average of the power levels in each fuel element type. Within the X-NTP model, each fuel element type and their associated amounts are considered in an average channel approximation per fuel element type. This results in not only a more accurate estimation of the temperature distribution, but also unlocks the preheating capability needed for alternative propellants. Each engine case that was evaluated had a different reactor power distribution curve that was calculated by OpenMC neutronics through the methodology shown in Figure 4.

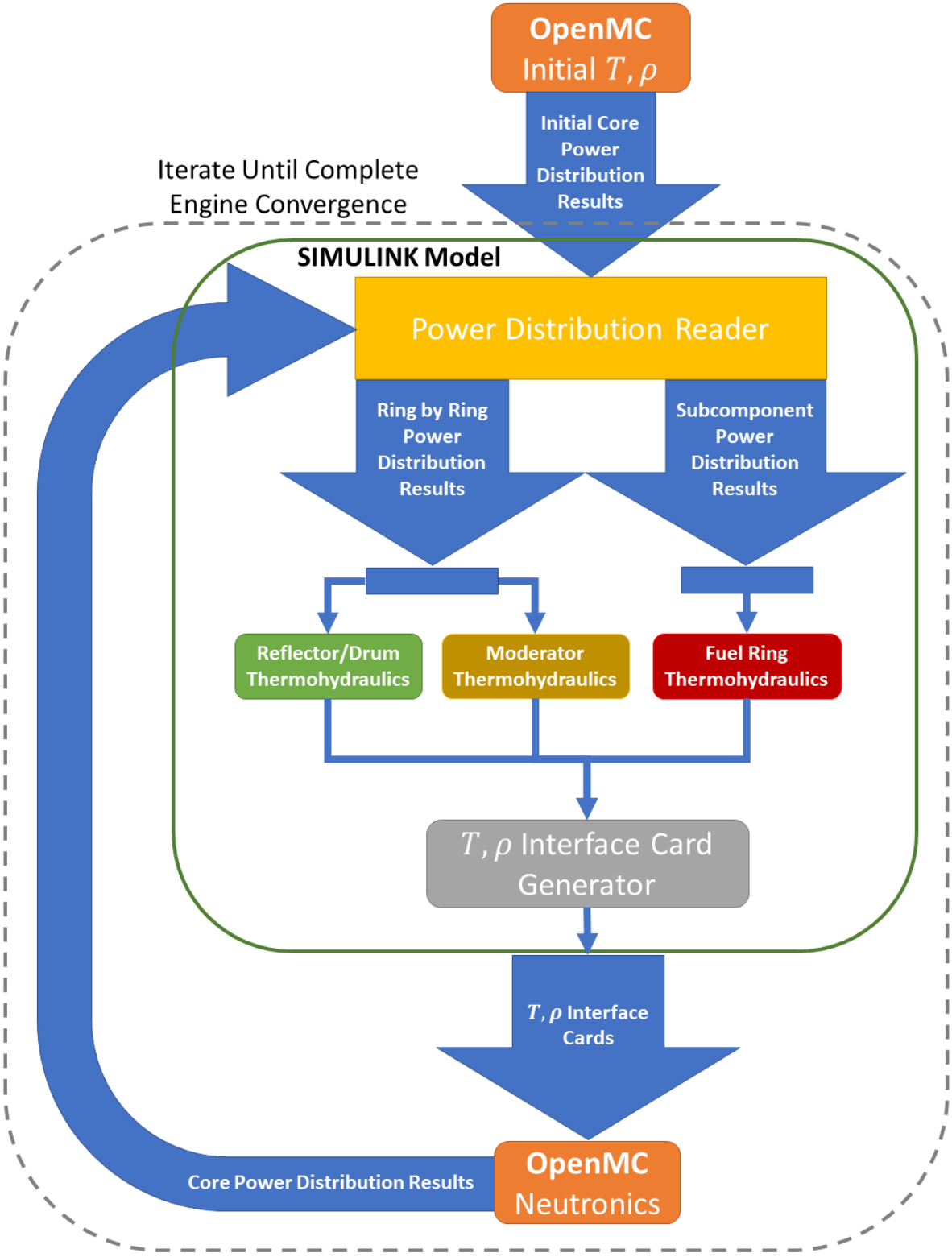

Figure 4: Iterative Procedure for the Reactor / Engine Algorithm for H-NTP and A-NTP

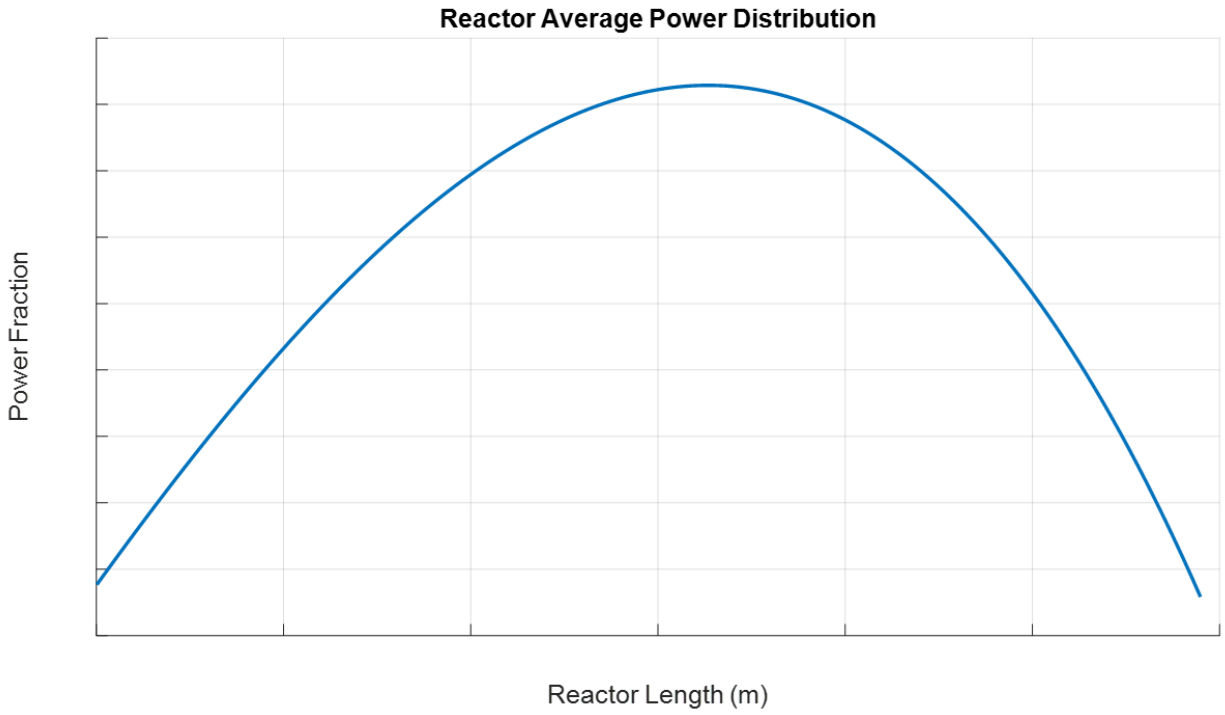

Figure 5: Example of an Average Power Distribution Curve

III. ENGINE CYCLE CONFIGURATION, ANALYSIS, AND RESULTS

This section will go through the details of both expander and bleed cycles and how they apply to both H-NTP and A-NTP engines. State by state walkthroughs of each cycle will be provided as well as the outputs from the X-NTP engine model. These outputs will then be compared and discussed. At the end of this section, recommendations will be provided regarding the best cycle for each propellant based on the model results. For all analysis cases, the criteria of convergence were set to be a maximum fuel temperature of 2850 K and a chamber pressure of 4.55 MPa which is consistent with the TRD [14] specifications. It should be noted that due to the nature of a simplified analysis from using the convective heat transfer coefficient method rather than numerical methods, the estimated results are conservative as the chamber temperature in none of the cases reach the specified 2700 K of the TRD.

A. Expander Cycle

The governing principle of an expander cycle is to incrementally expand the propellant after the pumps through the engine providing cooling and rerouting the turbine exhaust back into the chamber to provide thrust. This results in all the propellant going into the engine coming out of the nozzle instead of being wasted as turbine exhaust. In chemical engines, staged combustion can be implemented to drive the turbines by partially combusting a portion of the propellant. In monopropellant NTP systems, convective heat transfer will be required to provide enough enthalpy to the fluid to drive the turbines.

The left side of Figure 6 shows the H-NTP expander cycle from the TRD. The hydrogen flow starts out by exiting the propellant tank when the Pump Shut-Off Valve (PSOV) is opened and enters the Boost Pump at State 1. The Boost Pump is needed to prevent cavitation from

occurring at the inlet to the Main Pumps. A boost pump was not needed in the NERVA program since those were bleed cycles which did not require as high of a system pressure as the expander cycle.

The flow exits the Boost Pump and enters the Main Pumps at State 2 from which it exits at State 3 to go through the Pump Bypass Valve (PBV). From the PBV, the flow exits at State 4 and is split between the Moderator Element Control Valve (MECV) and the Regenerative cooling Control Valve (REGCV). From the exit of the REGCV at State 6, the flow provides regenerative cooling to the nozzle and exits at State 7 into the Control Drum/Reflector channels to also provide cooling and exits at State 8. From the exit of the MECV at State 10, the flow enters the Moderator Block cooling channels and exits at State 11. The exit flows from the Moderator Block and the Control Drum/Reflector region mix at State 12 and the flow is split between the Boost Turbine at State 13, the Main Turbines at State 15, and the Turbine Control Valve (TBCV) at State 17. The flows from the Boost Turbine, Main Turbines, and TBCV exit at States 14, 16, and 18, respectively and mix at State 19. The Turbine Valve (TBV) is used to provide additional pressure regulation to ensure robust control and throttlability of the engine by changing the turbine pressure ratio. The mixed flow at State 19 enters the Fuel Element Control Valve (FECV) and exits at State 20 to enter the Fuel Elements. The flow is superheated and exits at State 21 which corresponds to the chamber conditions. The flow then goes through the converging/diverging nozzle to become accelerated to provide thrust and exits the engine system at State 22. These state points have been summarized in Table 1. Many state points have been eliminated due to export compliance and the reader is advised to contact the primary author to obtain a full detailed table.

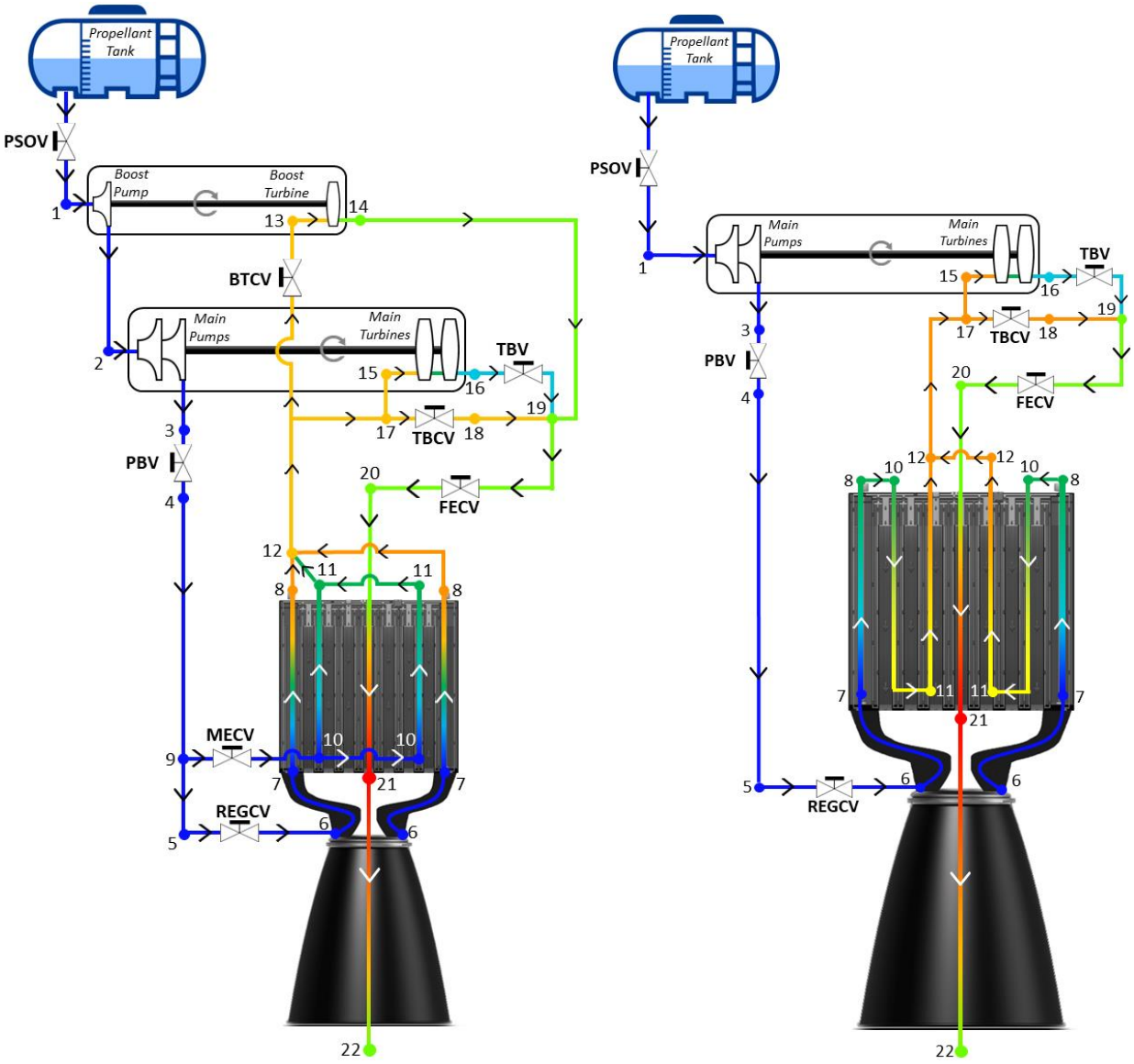

Figure 6: H-NTP (left) and A-NTP (right) Expander Cycle Engine Schematics

Table 1: H-NTP Expander Cycle State Points

State	ṁ (kg/s)	T (K)	P (MPa)
1	7.6320	20.0000	0.1391
2	7.6320	20.2533	0.3347
3	7.6320	37.9312	12.4254
4	7.6320	37.9406	12.3840
12	7.6320	271.4738	9.7984
21	7.6320	2563.7001	4.5500
22	7.6320	220.3507	0.0002

The right side of Figure 6 shows the ammonia A-NTP expander engine cycle. There are a few key differences between the H-NTP and A-NTP cycles. First, there is no boost pump or boost turbine due to ammonia's much wider liquid temperature range. Second, since ammonia's storage temperature and critical temperature are much farther apart than for hydrogen, additional preheating is required to provide a supercritical fluid to the turbines. Given the TRD reactor, to achieve this preheating, rings of fuel elements are isolated as preheating elements. To support the preheated propellant exiting at the top of the reactor, the flow is routed serially through the control drums and moderator block as opposed to parallel routing in the H-NTP expander cycle. Other elements such as the turbine circuit, valve placements, and flow schedule are the same as the H-NTP expander cycle.

Setting up the X-NTP model to run these two cycles revealed that ammonia A-NTP engines can have two modes: produce the same thrust as H-NTP or produce a higher thrust at the same reactor power level as H-NTP. The state points for both nodes are shown in Table 2 with the state points of the 15 klbf option on the left and the 330 MW option on the right. When compared to the state points of Table 1, it can be immediately recognized that the mass flow rate of the 15 klbf ammonia A-NTP option is nearly three times higher than that of H-NTP. Furthermore, both A-NTP cases exhibit higher pressures than that of H-NTP primarily due to two fundamental differences between the ammonia and hydrogen engine designs: (1) the addition of the preheating fuel elements reduces the effective cross sectional flow area of the superheating fuel elements and (2) ammonia requires a much higher pressure to become a supercritical fluid which is what is required to enter the turbines in the expander cycle version of the A-NTP engines.

Table 2: A-NTP Expander Cycle State Points

	15 klbf			330 MW		
State	**ṁ (kg/s)**	**T (K)**	**P (MPa)**	**ṁ (kg/s)**	**T (K)**	**P (MPa)**
1	19.2355	200.0000	0.1407	34.6561	200.0000	0.1163
3	19.2355	203.2564	13.9491	34.6561	203.3767	16.6846
4	19.2355	203.2601	13.9103	34.6561	203.3817	16.5939
12	19.2376	684.8103	11.6740	34.6561	688.4893	12.2040
21	19.2355	2551.8906	4.5503	34.6561	2424.6880	4.5038
22	19.2355	713.2021	0.0006	34.6561	674.2822	0.0010

The comparison of Key Performance Parameters (KPP) for expander cycle NTP engines are provided for the three cases in Table 3. It should be reiterated that the maximum fuel temperature was kept constant for all cases. As expected, the specific impulse of A-NTP is much lower than H-NTP, however, for the same thrust, the reactor power is also significantly lower. When the reactor power is increased in A-NTP to levels comparable with H-NTP, the thrust increases to over 25 klbf – characteristic of a higher thrust class for H-NTP, but which uses a reactor power level of 530 MW. Due to the increased density of ammonia and despite the higher flow rate, the shaft speed is lower in A-NTP than H-NTP resulting in lower radial stresses on the turbopump disks. Finally, a drawback that is more evident in maximizing the reactor power in A-NTP engine is the maximum system pressure which will require higher ducting mass to contain the elevated pressures.

Table 3: Expander Cycle NTP Engine KPP Comparison

Parameters	H-NTP	A-NTP 15 klbf	A-NTP $\dot{Q}_{max}$
$\dot{Q}_{tot}$ (MW)	311.1412	187.4790	322.2789
F (klbf)	15.3627	15.3458	25.6808
I_{sp} (s)	875.9682	355.5727	342.7755
$\dot{m}_{tot}$ (kg/s)	7.8162	19.2355	33.3888
$T_{fuel_{max}}$ (K)	2850.5689	2850.4370	2849.9268
$T_{chamber}$ (K)	2563.7001	2551.8906	2477.7849
ω_{shaft} (RPM)	37180.0408	15093.4390	19837.3499
$P_{sys_{max}}$ (MPa)	12.5224	13.9491	16.6846

B. Bleed Cycle

The bleed cycle was the first type of cycle to be used for rocket engines. The biggest advantage of using this cycle is to drive down the maximum system pressure. This comes at the expense of lower specific impulse which is caused by dumping a portion of the total propellant flow going through the turbines out of the engine without it providing any useable thrust. Since hydrogen has very a low critical temperature and pressure, the cycle is flexible in terms of bleeding hydrogen throughout parts of the engine to provide an accurate and stable turbine inlet temperature.

The left schematic of Figure 7 shows the H-NTP bleed cycle. There are noticeable differences between the H-NTP bleed and expander cycles. The first is that the bleed cycle no longer requires a Boost Pump due to the lower maximum system pressure. Furthermore, to adjust the turbine inlet temperature, two taps are used to mix the turbine inlet fluid. The first tap is from the Control Drum/Reflector and Moderator Cooling mixture and the second tap is from the chamber. Furthermore, the turbine exhaust is no longer routed back into the engine, but it is expelled. Table 4 shows the state points of the H-NTP bleed cycle. When State 3 is compared between the expander and bleed H-NTP cycles, it is evident that the bleed has a lower system pressure. As expected, H-NTP bleed cycle has a higher total mass flow rate which will drive the specific impulse down.

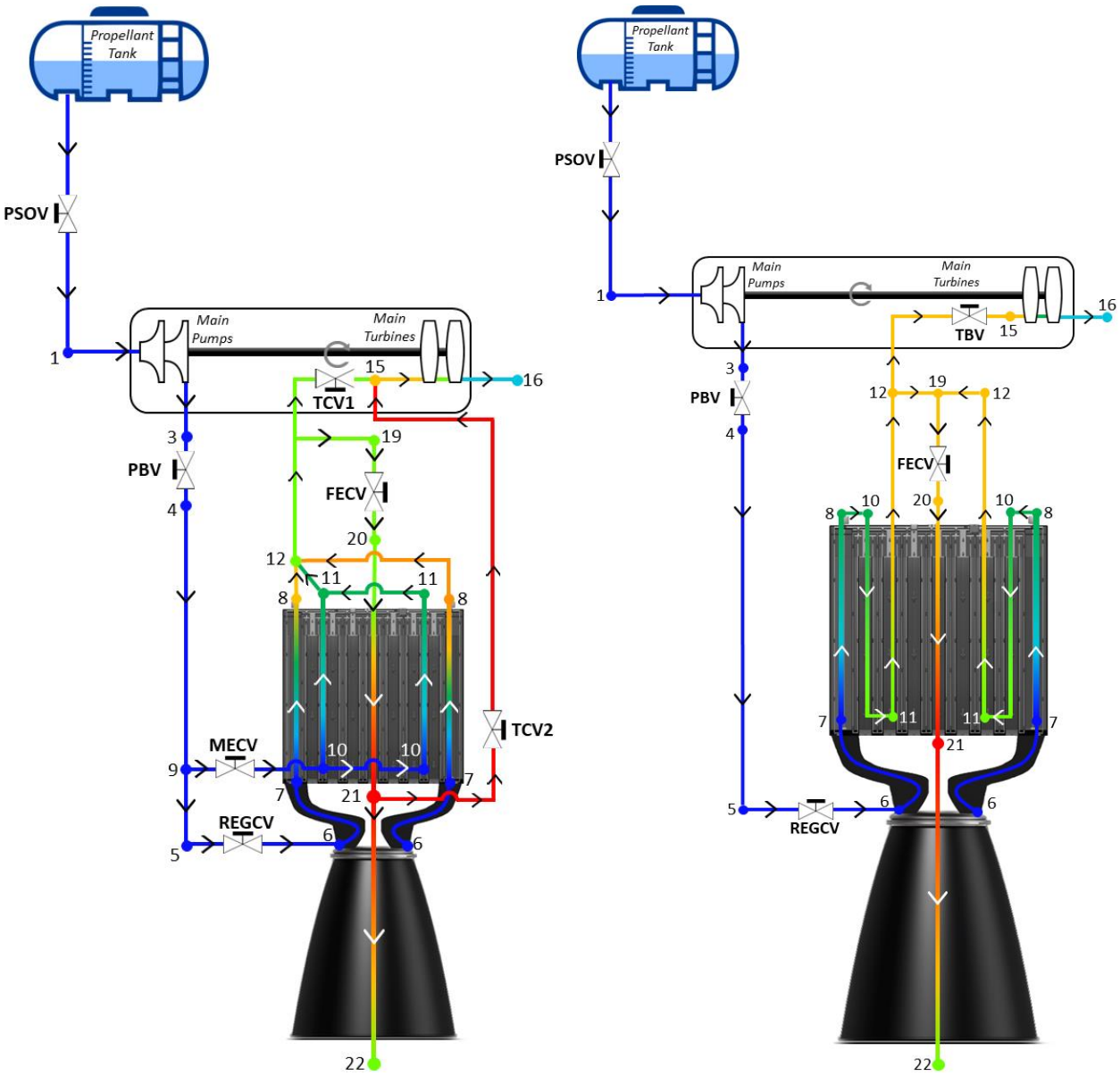

Figure 7: H-NTP (left) and A-NTP (right) Bleed Cycle Engine Schematics

Table 4: H-NTP Bleed Cycle State Points

State	ṁ (kg/s)	T (K)	P (MPa)
1	9.6433	20.0000	0.1326
3	9.6433	28.4113	9.2107
4	9.6433	28.4730	9.1633
12	9.6433	197.5947	8.0626
21	-	2484.6714	4.5505
22	-	211.7031	0.0002

The A-NTP bleed cycle significantly differs from the H-NTP bleed cycle in that the flow through the Control Drums/Reflector and Moderator Block are serial as well as the addition of the preheating elements as shown in the right schematic of Figure 7. Previous work considered only a hot bleed cycle for A-NTP which led to high turbine inlet temperatures and deemed infeasible [3]. Tap offs from other parts of the cycle were not possible due to the fluid state being liquid and preheating elements were not utilized. The A-NTP bleed cycle provided in this work is new as it does utilize preheating elements and a single tap-off point post preheating elements to use for the turbine inlet. This provides a similar turbine inlet temperature as is in the case of the expander cycle. Similar to the expander cycle analysis of A-NTP engines, two modes of operation were analyzed which include engine operation to provide 15 klbf and utilizing the maximum reactor power. The state points for both modes are shown in Table 5. When compared against the state points of Table 2, the difference in pressures is minor and does not provide a significant advantage over the A-NTP expander cycles. This is due to the increased mass flow rate resulting in higher pressure losses. As the pressure is reduced since the cycle does not need to accommodate from expanding flow through the turbines anymore, the density of the fluid decreases and increases the pressure losses further resulting in engine stall. Therefore, both expander and bleed cycle A-NTP engines must operate at similar maximum system pressures.

Table 5: A-NTP Bleed Cycle State Points

	15 klbf			**330 MW**		
State	**ṁ (kg/s)**	**T (K)**	**P (MPa)**	**ṁ (kg/s)**	**T (K)**	**P (MPa)**
1	20.7529	200.0000	0.1263	37.7774	200.0000	0.1125
3	20.7529	203.2980	14.1350	37.7774	202.9879	16.8832
4	20.7529	203.3017	14.0900	37.7774	202.9923	16.7857
6	20.7529	203.3017	14.0825	37.7774	202.9923	16.7651
12	20.7529	602.9521	11.3945	37.7774	614.4954	9.5047
21	-	2549.0001	4.5503	-	2484.1623	4.5361
22	-	711.6178	0.0006	-	791.6782	0.0012

When the H-NTP and A-NTP bleed cycle KPPs are compared side by side as they are in Table 6, it becomes evident that A-NTP requires significantly higher system pressures than H-NTP. The thrust values at the maximum reactor power level are comparable to those calculated for the expander cycle A-NTP. When the bleed cycle KPPs are compared against those of the expander cycles in Table 3, the mass flow rates are higher since a portion of that flow is allocated to the turbine bleed and the resulting specific impulse is lower uniformally across all examined cases. Furthermore, due to the higher system pressures and higher mass flow rates of the A-NTP engines, the shaft speed becomes comparable to that of H-NTP.

Table 6: Bleed Cycle NTP Engine KPP Comparison

Parameters	H-NTP	A-NTP 15 klbf	A-NTP $\dot{Q}_{max}$
$\dot{Q}_{tot}$ (MW)	305.1516	190.7102	327.2625
F (klbf)	15.1386	15.3449	26.0676
I_{sp} (s)	712.0514	317.5205	312.9819
$\dot{m}_{tot}$ (kg/s)	9.9305	21.9201	37.7774
$T_{fuel_{max}}$ (K)	2850.0903	2850.2527	2850.1557
$T_{chamber}$ (K)	2484.1623	2549.0001	2476.1623
ω_{shaft} (RPM)	40254	36519.9636	31833.5445
$P_{sys_{max}}$ (MPa)	9.2107	14.1350	16.8832

VI. CONCLUSION

An X-NTP engine model was coded in MATLAB's Simulink and the governing physics were summarized. The model logic was also discussed which has shown that this model is modular and capable of power balance analysis for various NTP engine cycles using different propellants. The focus of this work was comparing hydrogen and ammonia propellants and how the engines perform when expander and bleed cycles were analyzed. The assumptions that this work made included the same TRD reactor geometry and that different fuel loading will be sufficient to offset the difference in the neutronics caused by switching hydrogen to ammonia. This will result in less than optimum thermohydraulics in the reactor core for A-NTP, and therefore, the values presented in this work were assumed to be conservative.

This work concludes that it is advantageous from the point of view of system pressure, cycle simplicity, and potentially engine mass that H-NTP engines use the bleed cycle. Conversely, when the same is applied to A-NTP engines, the expander cycle is more advantageous. In terms of thrust performance , A-NTP engines functioning at the maximum reactor power level jump to a higher thrust class engine than H-NTP running at the same power level.

Future work will involve further analysis of the reactor neutronics and their impact on the power distributions found inside the reactor. Reactor geometry that departs from the TRD will also be analyzed and optimized for the different engine configurations. Directly coupling the execution of the Simulink model with reactor neutronics analysis software will provide a higher fidelity analysis and provide more realistic values.

APPENDIX: NOZZLE CONTOUR DERIVATION

Since the X-NTP model is modular and the convective heat transfer depends on the nozzle contour, it is important to review the derivation of the nozzle contour equation which has not been addressed by previous works. The input geometry variables are summarized in Table 1 which will be used as the constant values in this derivation. Furthermore, the geometric approximations that will be used for modeling the nozzle contour are shown in Figure 8. As can be seen, both the converging and diverging sections are modeled by quadratic equations with the throat modeled by

a circle. This modeling methodology provides a closed form solution with smooth geometry as well be discussed.

Table 7: Nozzle Contour Input Variables

Input Variable	Description
r_t	Throat radius
r_i	Nozzle inlet radius (radius of internal reactor diameter)
$r_{c_{regen}}$	Exit radius of the regenerative cooling section. It is important to differentiate that this is NOT the exit radius of the nozzle skirt.
L_c	Length of converging section from reactor exit to the middle of the throat.
L_d	Length of diverging section to the end of the regenerative cooling section. This is NOT until the end of the nozzle skirt.
θ	Angle the diverging section of the nozzle makes with the horizontal at the regenerative cooling exit.

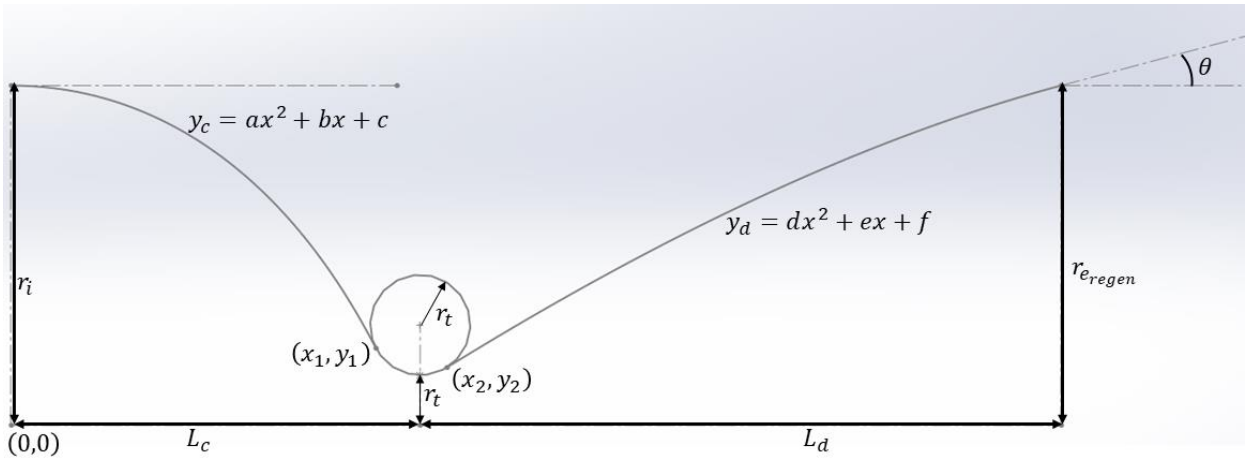

Figure 8: Nozzle Analytical Geometry

The goal of the solution is to solve for the parabola coefficients a, b, c, d, e, and f as well as where they meet the circle. The converging parabola y_c meets the circle at point (x_1, y_1) and the diverging parabola y_d meets the circle at point (x_2, y_2). At these points the parabolas are tangent to the circle.

A. Converging Parabola

A zoomed in view of the converging portion of the nozzle contour geometry is provided in Figure 9. Here, vectors have been added to estimate the (x_1, y_1) tangential point between y_c and the circle through angle α.

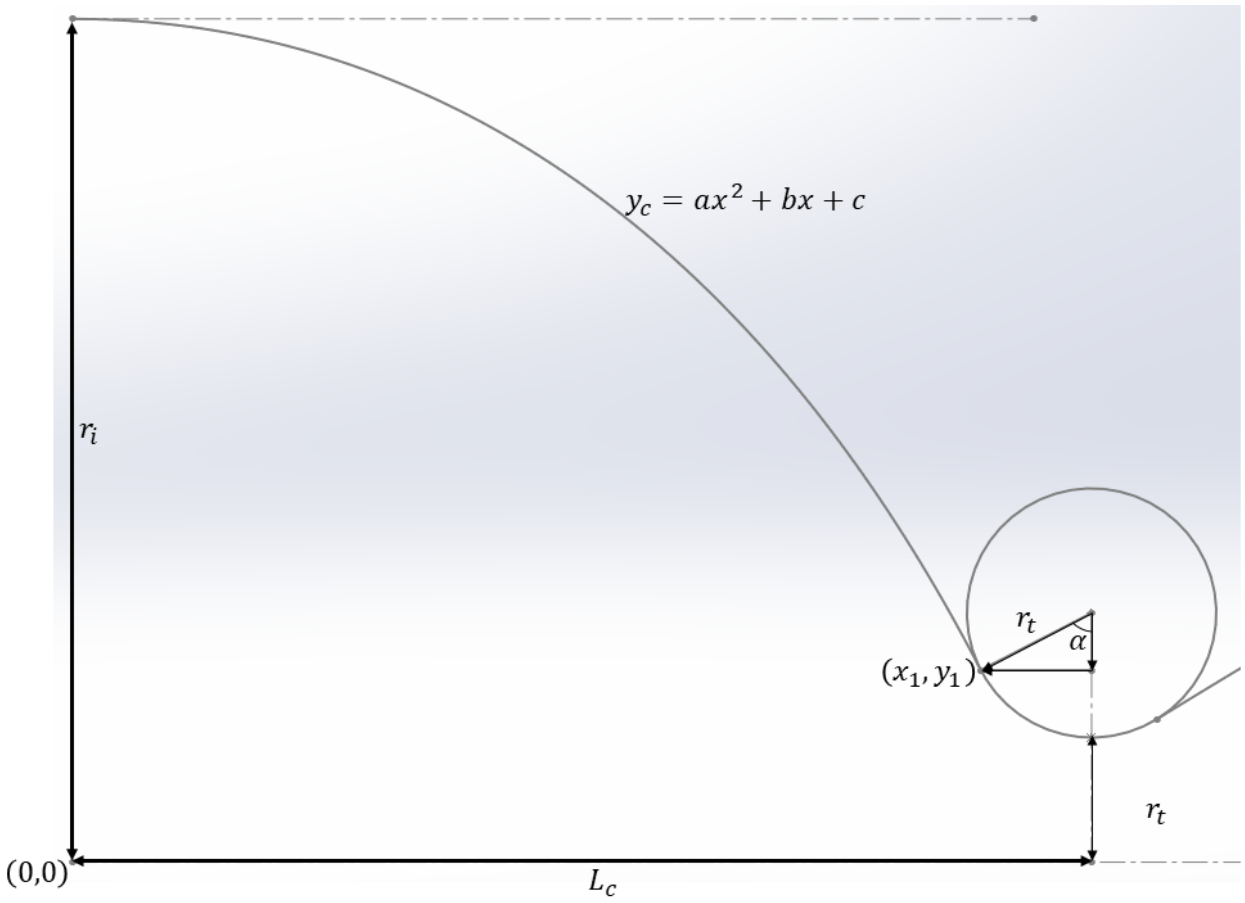

Figure 9: Converging Nozzle Geometry

The converging parabola y_c is defined by Eq. 25 and has the derivative $\frac{dy_c}{dx}$ shown in Eq. 26.

$$y_c = ax^2 + bx + c \quad \text{Eq. 25}$$

$$\frac{dy_c}{dx} = 2ax + b \quad \text{Eq. 26}$$

The circle is defined by Eq. 27 with the derivative shown in Eq. 28.

$$(x - L_c)^2 + (y - 2r_t)^2 = r_t^2 \quad \text{Eq. 27}$$

$$2(x - L_c) + 2(y - 2r_t)\frac{dy}{dx} = 0 \rightarrow \frac{dy}{dx} = \frac{L_c - x}{y - 2r_t} \quad \text{Eq. 28}$$

From trigonometry, as shown in Figure 9, using the angle α inside the circle, it follows that x_1 and y_1 can be defined by Eq. 29 and Eq. 30, respectively.

$$x_1 = L_c - r_t \sin(\alpha) \quad \text{Eq. 29}$$

$$y_1 = 2r_t - r_t \cos(\alpha) = r_t[2 - \cos(\alpha)] \quad \text{Eq. 30}$$

The converging parabola solution involves imposing boundary conditions on the parabola in Eq. 25 and its derivative in Eq. 26. These boundary conditions include linking: (1) Eq. 25 to r_i at $x = 0$ as shown in Eq. 31, (2) Eq. 25 to y_1 at x_1 as shown in Eq. 32, (3) Eq. 26 to 0 at $x = 0$ as shown in Eq. 33, and (4) Eq. 26 to Eq. 28 at x_1 as shown in Eq. 34.

(1) $$y_c(0) = r_i \quad \text{Eq. 31}$$

(2) $$y_c(x_1) = y_1 = r_t[2 - \cos(\alpha)] \quad \text{Eq. 32}$$

(3) $$\left.\frac{dy_c}{dx}\right|_0 = 0 \quad \text{Eq. 33}$$

(4) $$\left.\frac{dy_c}{dx}\right|_{x_1} = \frac{L_c - x_1}{y_1 - 2r_t} = \frac{L_c - L_c + r_t \sin(\alpha)}{r_t[2 - \cos(\alpha)] - 2r_t} = \frac{r_t \sin(\alpha)}{-r_t \cos(\alpha)} = -\tan(\alpha) \quad \text{Eq. 34}$$

This results in a system of 4 equations and 4 unknowns *a*, *b*, *c*, and α. Unfortunately, it is not advisable to input these equations into a solver as they will produce incorrect results. It is best to solve for *a*, *b*, and *c* analytically and combining them into a single transcendental equation in terms of α as shown in Eq. 35 which can then be solved numerically for α. The resulting converging parabola is shown in Eq. 36in terms of α.

$$r_t[2 - \cos(\alpha)] = r_i - \frac{\tan(\alpha)}{2}[L_c - r_t \sin(\alpha)] \quad \text{Eq. 35}$$

$$y_c = \frac{-\tan(\alpha)}{2[L_c - r_t \sin(\alpha)]} x^2 + r_i \quad \text{Eq. 36}$$

B. Diverging Parabola

Since the diverging section relies on the offset from the converging section, the length of the converging section must be accounted. Figure 10 shows the considered geometry for the diverging section as well as the vectors for point (x_2, y_2) and angle β between them.

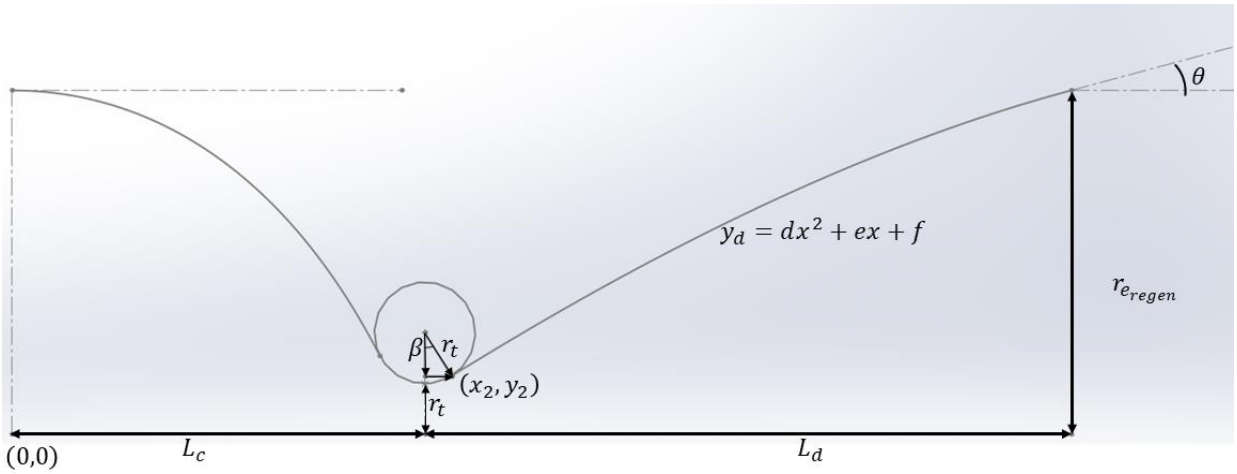

Figure 10: Diverging Nozzle Geometry

Similar to the converging section, the diverging parabola y_d and its derivative $\frac{dy_d}{dx}$ are defined in Eq. 37 and Eq. 38, respectively. The equation for the circle and its derivative are the same as were presented in Eq. 27 and Eq. 28, respectively.

$$y_d = dx^2 + ex + f \quad \text{Eq. 37}$$

$$\frac{dy_d}{dx} = 2dx + e \quad \text{Eq. 38}$$

From trigonometry, as shown in Figure 10, using the angle β inside the circle, it follows that $\boldsymbol{x_2}$ and $\boldsymbol{y}_2$ can be defined by Eq. 39 and Eq. 40, respectively.

$$x_2 = L_c + r_t \sin(\beta) \quad \text{Eq. 39}$$

$$y_2 = 2r_t - r_t \cos(\beta) = r_t[2 - \cos(\beta)] \quad \text{Eq. 40}$$

The diverging parabola solution involves imposing boundary conditions on the parabola in Eq. 37 and its derivative in Eq. 38. These boundary conditions include linking: (1) Eq. 37 to $r_{e_{regen}}$ at $x = L_c + L_d$ as shown in Eq. 41, (2) Eq. 37 to y_2 at x_2 as shown in Eq. 42, (3) Eq. 38 to $\tan(\theta)$ at $x = L_c + L_d$ as shown in Eq. 43, and (4) Eq. 38 to Eq. 28 at x_2 as shown in Eq. 44.

(1) $$y_d(L_c + L_d) = r_{e_{regen}} \quad \text{Eq. 41}$$

(2) $$y_d(x_2) = y_2 = r_t[2 - \cos(\beta)] \quad \text{Eq. 42}$$

(3) $$\left.\frac{dy_d}{dx}\right|_{L_c+L_d} = \tan(\theta)$$ Eq. 43

(4) $$\left.\frac{dy_d}{dx}\right|_{x_2} = \frac{L_c - x_2}{y_2 - 2r_t} = \frac{L_c - L_c - r_t\sin(\beta)}{r_t[2-\cos(\beta)] - 2r_t} = \tan(\beta)$$ Eq. 44

This again results in a system of 4 equations and 4 unknowns *d*, *e*, *f*, and β. The unknowns *d*, *e*, and *f* are analytically combined and expressed through a single transcendental equation in terms of β as shown in Eq. 45 which can be numerically solved. The resulting diverging parabola is shown in Eq. 46 in terms of β.

$$\begin{aligned} r_t[2-\cos(\beta)] &= \frac{\tan(\beta)-\tan(\theta)}{2[r_t\sin(\beta)-L_d]}[L_c + r_t\sin(\beta)]^2 \\ &+ \left[\tan(\theta) - 2\frac{\tan(\beta)-\tan(\theta)}{2[r_t\sin(\beta)-L_d]}(L_c+L_d)\right][L_c + r_t\sin(\beta)] \\ &+ \frac{\tan(\beta)-\tan(\theta)}{2[r_t\sin(\beta)-L_d]}(L_c+L_d)^2 \\ &+ \left[\tan(\theta) - 2\frac{\tan(\beta)-\tan(\theta)}{2[r_t\sin(\beta)-L_d]}(L_c+L_d)\right](L_c+L_d) - r_{e_{regen}} \end{aligned}$$ Eq. 45

$$\begin{aligned} y_d = \frac{\tan(\beta)-\tan(\theta)}{2[r_t\sin(\beta)-L_d]}x^2 &+ \left[\tan(\theta) - 2\frac{\tan(\beta)-\tan(\theta)}{2[r_t\sin(\beta)-L_d]}(L_c+L_d)\right]x \\ &+ \frac{\tan(\beta)-\tan(\theta)}{2[r_t\sin(\beta)-L_d]}(L_c+L_d)^2 \\ &+ \left[\tan(\theta) - 2\frac{\tan(\beta)-\tan(\theta)}{2[r_t\sin(\beta)-L_d]}(L_c+L_d)\right](L_c+L_d) - r_{e_{regen}} \end{aligned}$$ Eq. 46

ACKNOWLEDGMENTS

This work was supported by NASA's Space Technology Mission Directorate (STMD) through the Space Nuclear Propulsion (SNP) project. This work was funded under Contract No. 80LARC17C0003. This research made use of Idaho National Laboratory computing resources which are supported by the Office of Nuclear Energy of the U.S. Department of Energy and the Nuclear Science User Facilities under Contract No. DE-AC07-05ID14517.

REFERENCES

[1] Robbins, W. H., and Finger, H. B. *An Historical Perspective of the NERVA Nuclear Rocket Engine Technology Program*. Publication NASA-CR-187154. Analytical Engineering Corporation, 1991.

[2] Emrich, W. *Principles of Nuclear Rocket Propulsion*. Butterworth-Heinemann, an imprint of Elsevier, Oxford, United Kingdom, 2016.
[3] Nikitaev, D., and Thomas, D. L. "Alternative Propellant Nuclear Thermal Propulsion Engine Architectures." *Journal of Spacecraft and Rockets*, 2022, pp. 1–11. https://doi.org/10.2514/1.A35289.
[4] Thermophysical Properties of Fluid Systems. National Institute of Standards and Technology (NIST), , 2022.
[5] Nikitaev, D., and Dale Thomas, L. "Impacts of In Situ Alternative Propellant on Nuclear Thermal Propulsion Mars Vehicle Architectures." *Journal of Spacecraft and Rockets*, Vol. 59, No. 6, 2022, pp. 2038–2052. https://doi.org/10.2514/1.A35399.
[6] Nikitaev, D. *Seeding Hydrogen Propellant in Nuclear Thermal Propulsion Engines*. Thesis. University of Alabama in Huntsville, Huntsville, AL, 2019.
[7] Nikitaev, D. *Implications of Alternative In-Situ Propellants Used in Nuclear Thermal Propulsion Engines*. Dissertation. University of Alabama in Huntsville, Huntsville, AL, 2021.
[8] Nikitaev, D., and Thomas, L. D. "Seeded Hydrogen in Nuclear Thermal Propulsion Engines." *Journal of Spacecraft and Rockets*, Vol. 57, No. 5, 2020, pp. 907–917. https://doi.org/10.2514/1.A34711.
[9] Nikitaeva, D., Smith, C., D., and Duchek, M. Effects of Heat Transfer Coefficient Variation on Nuclear Thermal Propulsion Engine Performance. Idaho Falls, ID, 2023.
[10] Emrich, W. Jr. *Principles of Nuclear Rocket Propulsion*. Butterworth-Heinemann, Kidlington, Oxford, United Kingdom, 2016.
[11] Bell, I. H., Wronski, J., Quoilin, S., and Lemort, V. "Pure and Pseudo-Pure Fluid Thermophysical Property Evaluation and the Open-Source Thermophysical Property Library CoolProp." *Industrial & Engineering Chemistry Research*, Vol. 53, No. 6, 2014, pp. 2498–2508. https://doi.org/10.1021/ie4033999.
[12] Nikitaev, Dennis, Smith, Corey D., and Palomares, Kelsa. Summary of the Comparison of Convective Heat Transfer Correlations. Cleveland, OH, 2022.
[13] Gustafson, J., Kreicicki, M., Swanson, R., Zilka, B., and Witter, J. K. Space Nuclear Propulsion Fuel and Moderator Development Plan Conceptual Testing Reference Design. Virtual Event, 2021.